ANALYSIS OF TWO-ELEMENT HIGH LIFT SYSTEMS IN TRANSONIC FLOW

Bert G. Arlinger

Aerospace Division, Saab-Scania AB, Linköping,Sweden

Abstract

A calculation method has been developed for the two-dimensional inviscid transonic flow around two-element airfoil systems, such as an airfoil with a leading-edge slat or a trailing-edge flap. Using a conformal mapping sequence the flow field is mapped to an annular domain where the two circles represent the two airfoil contours. The full potential equation is solved in this domain using a symmetric successive line overrelaxation procedure.

Calculated results are presented for various configurations and Mach numbers. Comparisons are also made with some available experimental results which, however, show large viscous effects.

1. Introduction

Since Murman and Cole[1] introduced the mixed central and upwind difference schemes in numerical transonics various efficient methods have been developed for transonic flow around single airfoils[2,3]. The case involving two elements in transonic flow makes an analysis much more complicated. This configuration is, however, of great interest for the aerodynamicist wanting to improve aircraft maneuverability in the transonic speed regime using a leading edge slat or a slotted trailing edge flap.

A calculation method based on small-disturbance theory for the transonic two-element problem has been presented by Caughey[4]. The slat boundary conditions were applied along a streamline in the incompressible flow about the main airfoil, an approximation which might imply small or large differences from the real flow depending on the configuration.

An essential problem for the accurate treatment of the two-element case is the design of a suitable coordinate system. Conformal mapping technique has proved to be a good tool for various configurations such as single airfoils[2,3] and nacelles[5,6]. For the two-element case Ives[7] developed a conformal mapping where the whole flow field was mapped to the region between two concentric circles. This mapping has been used in a very recent paper by Grossman and Melnik[8] and in the present work. Because in both cases the full potential equation is solved for arbitrary two-element configurations using the same type of coordinate system, the two methods are similar in many respects although they have been developed independently.

The present work was initiated as a result of a mutual interest from Dornier GmbH in Germany and Saab-Scania to improve the computational capability in the field of transonic high lift systems.

A coordinate system created by conformal mapping was chosen because it generally simplifies both the boundary conditions and the equation. However, the fact that the infinity is mapped to a point in the annular region results in extensive algebraic expressions in the final equation for the reduced potential, and also causes some numerical problems due to large discretization errors close to the infinity point. The equation for the reduced potential is solved numerically by type-dependent line relaxation, sweeping the annular region in both circumferential directions using a rotated upwind difference scheme in supersonic regions.
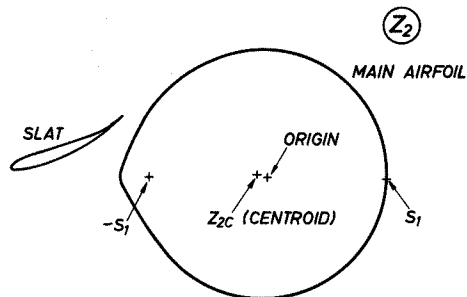
The numerical schemes are written in non-conservative form. Although this is known to give errors in shock jumps and locations compared to a fully conservative formulation[9,10], it was considered adequate at the present stage, because the omission of all viscous effects probably has greater influence on the pressure distribution for many two-element configurations.
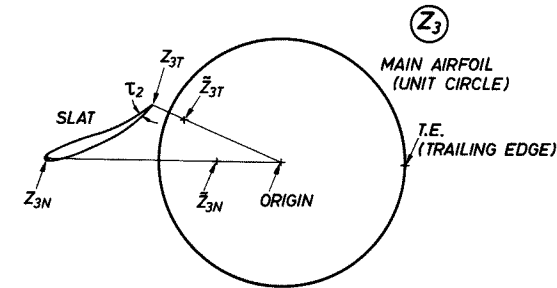
2. The mapping

The sequence of mappings leading from the physical plane to the annulus is shown in Fig. 1 for a case with leading edge slat. The mapping is essentially the one derived by Ives[7], where a more detailed discussion of the various stages can be found.

$$\frac{Z_2 - S_1}{Z_2 + S_1} = \left(\frac{Z_1 - Z_{1T}}{Z_1 - Z_{1N}}\right)^{1/K_1}$$

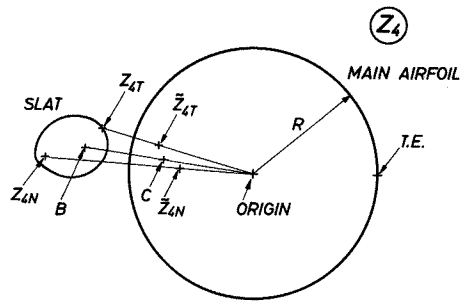$$S_1 = (Z_{1T} - Z_{1N})/(2K_1)$$

$$K_1 = 2 - \tau_1/\pi$$

$$Z_2 - Z_{2C} = Z_3 \ e^{\sum_{j=0}^{N_1} (A_j + iB_j) Z_3^{-j}}$$

Left column figures:

(z_3)

SLAT

MAIN AIRFOIL
(UNIT CIRCLE)

z_{3T}
τ_2
$\tilde{z}_{3T}$

T.E.
(TRAILING EDGE)

z_{3N} $\tilde{z}_{3N}$ ORIGIN

$|z_{3T} \cdot \tilde{z}_{3T}| = 1$
$|z_{3N} \cdot \tilde{z}_{3N}| = 1$
$|z_{4T} \cdot \tilde{z}_{4T}| = R^2$
$|z_{4N} \cdot \tilde{z}_{4N}| = R^2$
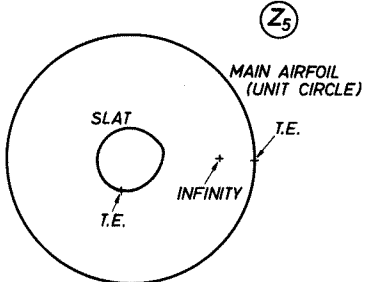$K_2 = 2 - \tau_2/\pi$

$$\frac{z_4 - z_{4T}}{z_4 - z_{4N}} \cdot \frac{z_4 - \tilde{z}_{4T}}{z_4 - \tilde{z}_{4N}} = \left(\frac{z_3 - z_{3T}}{z_3 - z_{3N}} \cdot \frac{z_3 - \tilde{z}_{3T}}{z_3 - \tilde{z}_{3N}} \right)^{1/K_2}$$
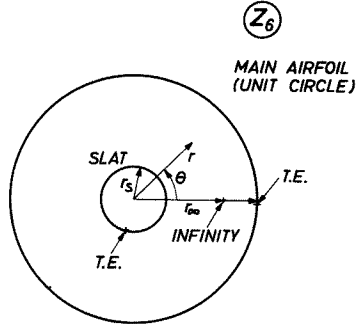
(z_4)

SLAT

MAIN AIRFOIL

z_{4T} $\tilde{z}_{4T}$ R

T.E.

z_{4N} B   C $\tilde{z}_{4N}$ ORIGIN

$$z_5 = A \frac{z_4 - B}{z_4 - C}$$ $|B \cdot C| = R^2$

(z_5)

MAIN AIRFOIL
(UNIT CIRCLE)

SLAT

T.E.

INFINITY

T.E.

$$z_5 = z_6 \, e^{\sum_{j=0}^{N_2} \left[(-C_j + iD_j)(r_s z_6)^j + (C_j + iD_j)(r_s/z_6)^j \right]}$$

(z_6)

MAIN AIRFOIL
(UNIT CIRCLE)

SLAT r_s r θ T.E.

r_∞

INFINITY

T.E.

Fig. 1   The mapping sequence for a leading edge slat configuration.

Right column text:

A main contribution by Ives is the mapping step from z_3 to z_4 where the slat contour is transformed to a near circle while the main airfoil circle is kept a circle. To show that the transformation has the latter property requires some analysis, but the fact that image points with respect to the circles are used suggests the following alternative formulation of the transformation

$$\frac{z_4 - z_{4T}}{z_4 - \tilde{z}_{4T}} \cdot \frac{z_4 - \tilde{z}_{4N}}{z_4 - z_{4N}} = \left(\frac{z_3 - z_{3T}}{z_3 - \tilde{z}_{3T}} \cdot \frac{z_3 - \tilde{z}_{3N}}{z_3 - z_{3N}} \right)^{1/k_2} \quad (1)$$

Because of the properties of image points it is obvious that the absolute value of both sides is constant when z_4 and z_3 are on the circles. Also the argument variation of both sides is continous for the circles. Thus the transformation (1) should map the z_3 unit circle to a circle in z_4 and also effect the slat contour in the same way as Ives transformation.

Writing either of these two transformations as

$$F_4(z_4) = \left[F_3(z_3) \right]^{1/k_2}$$

the further conditions needed for determining the constants in the transformations are

$$\frac{dz_3}{dz_4} \rightarrow 1 \quad \text{as} \quad z_3, \ z_4 \rightarrow \infty \quad (2)$$

$$F_4(z_{4,s}) = \left[F_3(z_{3,s}) \right]^{1/k_2} \ ; \quad s = 1,2 \quad (3)$$

$z_{i,s}$ are the two singular points determined by

$$\frac{dF_i}{dz_i} = 0$$

and which are located on the circles for both transformations.

The computational plane is denoted z_6 in Fig. 1 and is rotated so that the infinity point is located on the positive real axis. A simple polar coordinate system (r, Θ) is used in this plane.

Fig. 2 illustrates the correspondence between the grids in the computational and physical planes. Indices attached to a few grid lines make the relationship between the planes more clear. It is suitable for the mesh point distribution in the physical plane to use non-equidistant spacing in r and Θ.

The calculation of this rather complex mapping requires only moderate computer times. This is mainly because fast Fourier transform technique is used in the iterative sequences for calculating the series coefficients in the $z_2 \rightarrow z_3$ and $z_5 \rightarrow z_6$ transformations. As an example, a mapping using 112 terms in the two series (N_1 and $N_2 = 112$) required only 8 seconds on a CDC 6600. The calculation of the mapping modulus $|dz_1/dz_6|$ for all mesh points, which is performed after that, generally requires more time.
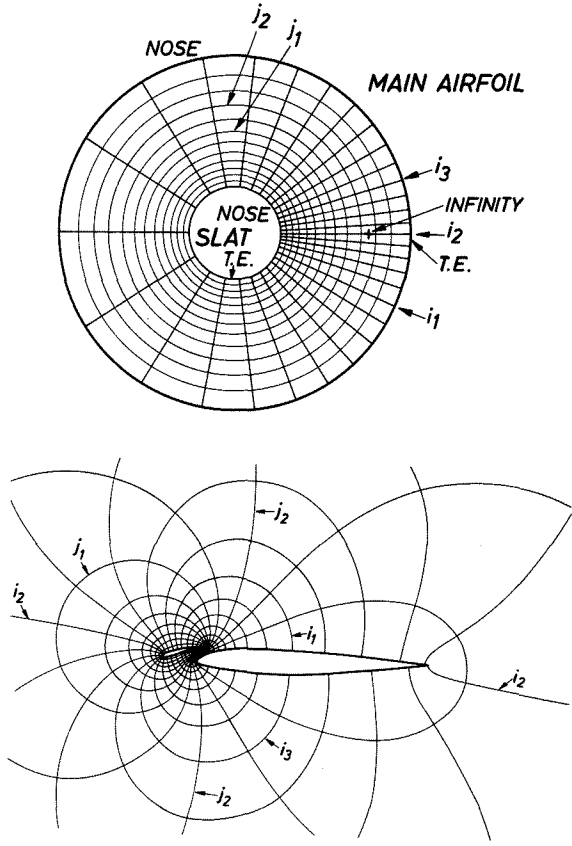
Fig. 2 Corresponding grids in the computational and physical planes.

3. Flow analysis

Basic formulation

The potential equation transformed to the polar coordinate system in the computational plane is

$$(a^2-q_1^2)\phi_{rr} - \frac{2q_1 q_2}{r}\phi_{r\theta} + \frac{a^2-q_2^2}{r^2}\phi_{\theta\theta} + \frac{a^2+q_2^2}{r}\phi_r$$

$$+ q^2 \left(q_1 B_r + q_2 \frac{1}{r} B_\theta\right) = 0 \qquad (4)$$

where ϕ is the velocity potential, q the absolute value of the velocity with the radial and circumferential components q_1 and q_2, a the sound velocity and B the mapping modulus. The following relations apply

$$q_1 = \frac{1}{B}\phi_r \qquad (5a)$$

$$q_2 = \frac{1}{Br}\phi_\theta \qquad (5b)$$

$$a^2 = \frac{1}{M_\infty^2} + \frac{\gamma-1}{2}(1-q^2) \qquad (6)$$

$$B = \left|\frac{dz_1}{dz_6}\right| \qquad (7)$$

where M_∞ is the free stream Mach number and the free stream value of q is set equal to 1.

The boundary conditions of zero normal velocity along the two circles give

$$\phi_r = 0 \qquad \text{for } r = r_s, 1 \qquad (8)$$

where r_s is the inner circle radius.

The mapping modulus B goes to zero at the two trailing edge points, so the requirement of no flow around the trailing edges gives the Kutta conditions

$$\phi_\theta = 0 \qquad \text{at the t.e. points} \qquad (9)$$

The reduced potential

Instead of the potential ϕ which is unbounded and many-valued, a reduced potential is introduced for use in the numerical calculations. First, the terms are subtracted from ϕ which account for the undisturbed and circulatory flow close to infinity. In the physical z_1-coordinates these well-known far field potentials are

$$f_1 = \text{Re}\,(z_1\,e^{-i\alpha}) \qquad (10)$$

$$f_2 = -\frac{\Gamma_m+\Gamma_s}{2\pi}\,tg^{-1}\left[\beta tg\,(\theta_1-\alpha)\right] \qquad (11)$$

Here α is the angle of attack relative to the x_1-axis, Γ_m and Γ_s are the circulations for the main and secondary airfoil respectively, θ_1 is the polar angle in the z_1-plane and $\beta = \sqrt{1-M^2}$. The expression (11) is originally due to Ludford[11].

Close to the infinity point the mapping is of the form

$$z_1 = \frac{a_1\,e^{ia_2}}{re^{i\theta} - r_\infty} + 0(1) \qquad (12)$$

where a_1 and a_2 are real constants calculated in the mapping procedure and r_∞ is the z_6-coordinate for the infinity point.

Rewriting f_1 and f_2 in the computational variables r,θ with the use of Eq. (12) without the $0(1)$ terms, then yields

$$f_1 = a_1\frac{S}{\sigma^2} \qquad (13)$$

$$f_2 = \frac{\Gamma_m + \Gamma_s}{2\pi}\,tg^{-1}\left(\beta\frac{T}{S}\right) \qquad (14)$$

with

$$S = c_1\,(r\cos\theta - r_\infty) + s_1\,r\sin\theta \qquad (15a)$$

$$T = c_1\,r\sin\theta - s_1\,(r\cos\theta - r_\infty) \qquad (15b)$$

$$c_1 = \cos\,(a_2-\alpha) \qquad (16a)$$

$$s_1 = \sin\,(a_2-\alpha) \qquad (16b)$$

$$\sigma^2 = r^2 + r_\infty^2 - 2r\,r_\infty\cos\theta \qquad (17)$$

where σ is the distance from a point r,θ to the infinity point.

A third term has to be introduced to get a single-valued reduced potential

$$f_3 = - \frac{\Gamma_s}{2\pi} \theta \qquad (18)$$

The function $f_2 + f_3$ gives the proper potential jumps Γ_m and Γ_s for paths around each of the airfoils and $\Gamma_m + \Gamma_s$ for paths including both airfoils. This is easily seen when considering the corresponding paths in the computational plane, for instance deduced from Fig. 1 or Fig. 2.

Thus a suitable reduced potential should be

$$\chi = \phi - (f_1 + f_2 + f_3)$$

However, it was found convenient to introduce another function. The reason for this is the fact that all the boundary conditions are of Neumann type, i.e. the flux due to χ is prescribed along all the boundaries. This situation might be expected to cause numerical problems, because the two sides in Gauss' relation often will not match exactly due to discretization errors. That means, that the total flux created in the field, as given by the Poisson term in the equation, is not exactly equal to the total flux through the boundaries, as prescribed by the boundary conditions.

Numerical problems in the form of very slow convergence rates were encountered already for incompressible test cases. They were cured by the introduction of a part of the analytical solution for $M_\infty = 0$, satisfying the boundary conditions

$$(f_{1_r})_s + f_{4_r} = 0 \qquad \text{for } r = r_s, 1 \qquad (19)$$

where $(f_{1_r})_s$ is the part of f_{1_r} which is symmetrical in θ. This arrangement yields smaller discretization errors along the boundaries and in the flow field by eliminating large circumferential variations in χ_r along the boundaries caused by $(f_{1_r})_s$. The new boundary conditions, obtained from Eqs. (8) and (19), are

$$\chi_r = -(f_{1_r})_a - f_{2_r} \qquad \text{for } r = r_s, 1 \qquad (20)$$

for the reduced potential

$$\chi = \phi - (f_1 + f_2 + f_3 + f_4) \qquad (21)$$

Here $(f_{1_r})_a$ is the antisymmetrical part of f_{1_r}. The function f_4 is a solution of Laplace's equation

$$f_4 = \sum_{k=1}^{N} (d_k r^k + d_{-k} r^{-k}) \cos k\theta \qquad (22)$$

with the coefficients d_k and d_{-k} determined using Eq. (19), yielding

$$d_k = \frac{a_1 c_1}{r_\infty} \left[\left(\frac{r_\infty}{r_s}\right)^k - \left(\frac{r_s}{r_\infty}\right)^k \right] \frac{1}{r_s^{-k} - r_s^{k}} \qquad (23a)$$

$$d_{-k} = \frac{a_1 c_1}{r_\infty} \left[(r_s r_\infty)^k - \left(\frac{r_s}{r_\infty}\right)^k \right] \frac{1}{r_s^{-k} - r_s^{k}} \qquad (23b)$$

The equation for the reduced potential

Having regularized the mapping modulus close to infinity by introducing

$$H = \sigma^2 B \qquad (24)$$

the equation for the reduced potential can be written

$$D\chi + DF + \frac{q^2}{\sigma^2} \left[q_1 H_r + \frac{q_2}{r} H_\theta - 2q_1 \frac{H}{\sigma^2} (r - r_\infty \cos\theta) \right.$$
$$\left. - 2q_2 \frac{H}{\sigma^2} r_\infty \sin\theta \right] = 0 \qquad (25)$$

where D is the differential operator in Eq. (4)

$$D = (a^2 - q_1^2) \frac{\partial^2}{\partial r^2} - \frac{2q_1 q_2}{r} \frac{\partial^2}{\partial r \partial \theta} + \frac{a^2 - q_2^2}{r^2} \frac{\partial^2}{\partial \theta^2}$$
$$+ \frac{a^2 + q_2^2}{r} \frac{\partial}{\partial r} \qquad (26)$$

and

$$F = f_1 + f_2 + f_3 + f_4 \qquad (27)$$

The velocity components are

$$q_1 = \frac{\sigma^2}{H} (F_r + \chi_r) \qquad (28a)$$

$$q_2 = \frac{\sigma^2}{Hr} (F_\theta + \chi_\theta) \qquad (28b)$$

Close to the infinity point these expressions become

$$q_1 = -\cos(2\Psi - a_2 + \alpha) + 0(\sigma) \qquad (29a)$$

$$q_2 = -\sin(2\Psi - a_2 + \alpha) + 0(\sigma) \qquad (29b)$$

where Ψ is the angle to the infinity point, i.e.

$$tg\,\Psi = \frac{r\sin\theta}{r\cos\theta - r_\infty} \qquad (30)$$

The boundary conditions are given in Eq. (20), and from Eqs. (9),(14),(18) and (21) the Kutta condition can be written

$$\Gamma_m \tilde{f}_{2_\theta} + \Gamma_s \left(\tilde{f}_{2_\theta} - \frac{1}{2\pi} \right) = -\chi_\theta - f_{1_\theta} - f_{4_\theta} \qquad (31)$$

with

$$f_{2_\theta} = (\Gamma_m + \Gamma_s) \tilde{f}_{2_\theta}$$

Eq. (31) is evaluated at the two trailing edge points yielding two linear equations for the two unknowns Γ_m and Γ_s.

4. Finite difference procedure

Rotated scheme

The streamlines in the computational plane for a slatted airfoil case are shown in Fig. 3. It is clear from the figure, that in supersonic regions a rotated difference scheme must be used, so that a locally correct upwind differencing is obtained.
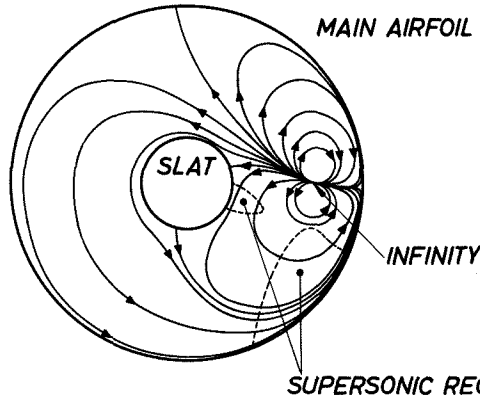

Fig. 3 Streamline pattern in the computational plane for a leading edge slat configuration.

The rotated scheme is obtained in the usual way, introduced by Jameson[12], by grouping the second order derivatives of χ in two parts, one representing streamwise differentiation and the other normal differentiation. In the present case this gives

$$(a^2 - q_1^2)\chi_{rr} - 2\frac{q_1 q_2}{r}\chi_{r\theta} + \frac{a^2 - q_2^2}{r^2}\chi_{\theta\theta} =$$

$$(a^2 - q^2)\frac{1}{q^2}\left[q_1^2\chi_{rr} + 2\frac{q_1 q_2}{r}\chi_{r\theta} + \frac{q_2^2}{r^2}\chi_{\theta\theta}\right]$$

$$+ a^2\frac{1}{q^2}\left[q_2^2\chi_{rr} - 2\frac{q_1 q_2}{r}\chi_{r\theta} + \frac{q_1^2}{r^2}\chi_{\theta\theta}\right]$$

$$= (a^2 - q^2)\chi_{ss} + a^2\chi_{nn} + 0\ (\chi_s, \chi_n) \qquad (32)$$

Thus, in supersonic regions upwind differences are used for all terms in the first square bracket and central differences for all terms in the second square bracket.

Grid system and sweep pattern

One grid line was always located along the real axis passing through the infinity point. The varying grid spacing around the circumference was controlled by an analytic expression relating θ to an angle θ' for which equidistant spacing was applied.

In the radial direction a logaritmic grid line distribution was used, i.e. dr is proportional to r. The grid was chosen so that the infinity point was not too close to a grid point.

The problem of finding a suitable sweep pattern for the relaxation procedure can be solved in various ways. To get a simple updating system working for all cases a symmetric successive overrelaxation system was chosen by updating lines of constant θ, sweeping back and forth in circumferential direction. When sweeping through supersonic regions, the reduced potential was updated only if the sweep direction was less than 90 degrees different from the flow direction, otherwise the potential in the supersonic points was kept unchanged. Thus, each supersonic point was updated once and each subsonic point twice in a complete back and forth sweep.

The sweep starting and reversing line can be chosen freely. In most cases it was located somewhere around $\theta = 90^\circ$ in order not to interfere with the infinity and trailing edge regions.

The Kutta conditions, Eq. (31), were applied after each flow field sweep. Because the trailing edge points generally do not coincide with grid points, linear interpolation was used for χ_θ.

The infinity region

The numerical difficulties that might occur when Neumann conditions are prescribed for all the boundaries become apparent again for Mach numbers greater than 0. This is because all terms in the potential equation (25) then become significant, many of which are heavily varying close to the infinity point. Although the reduced potential χ is single-valued and bounded at the infinity point, this is not the case for $D\chi$ which is unbounded for z_6 approaching the infinity point. Thus the discretization errors are expected to be large in a region around the infinity point, although analytical expressions are used for evaluating all terms in DF in Eq. (25). The numerical effect of this is, that the maximum residual (i.e. the largest error in the difference equation) does not converge to any prescribed small amount but gradually assumes a constant value.

It should be noted that increasing errors in χ when approaching the infinity point normally do not mean increasing errors in the velocity components, because the contribution from χ to q_1 and q_2 is of order σ^2 close to the infinity point, while the leading terms are of order 1 and σ as seen from Eqs. (29a) and (29b).

To improve the convergence in the relaxation procedure, Dirichlet type boundary conditions were introduced along a small grid rectangle enclosing the infinity point. This was done by freezing the potential values on the grid rectangle after the initial iteration phase did not converge any more. Then, continued iterations on the annulus with the region around the infinity point excluded gives convergence to any prescribed level (slower for smaller regions around the infinity point).

This can be regarded as applying a sort of far field conditions. The changes in velocities and circulations during the second iteration phase were generally small, for instance less than 2 % in the circulations for typical cases.

Another way of improving the convergence, which has not been tried, would be to get rid of the numerically generated sources in the flowfield by solving the potential equation in fully conservative form.

Grossmann and Melnik[8] do not report convergence problems of the type encountered here. They use the same equation with the same reduced potential except for f_4, but a different sweep system. Their approach of having a grid point coinciding with the infinity point with prescribed potential can be regarded as a weaker version of the present approach of freezing the potential in a few points around the infinity.

5. Results

Most of the calculations presented here were made on a grid with 40x60 points in the radial and circumferential directions respectively. The computations were made with a program which is not very optimized and has no mesh refinement capability, so the typical computing times of 5-10 minutes on CDC 6600 are expected to be reduced for a more efficient program version.

The program works both for airfoils with leading edge slats and trailing edge flaps, but because of a greater current interest in the leading edge slat configurations, these dominate the results.

In Fig. 4 a comparison is made between the present method and a Douglas-Neumann calculation for the incompressible flow around a NACA 65_2-215 with a leading edge slat. The discrepancies in the pressure for the rear part of the slat are probably the result of too few panels in this region in the Douglas-Neumann calculation.

There seems to be a lack of experimentally determined pressure distributions for two-element configurations in transonic flow without too large viscous effects. The experimental results shown in Figs. 5 and 6 for Mach numbers 0.6 and 0.7 were obtained for an airfoil-slat configuration, denoted F1.1, developed at Dornier GmbH. The wind tunnel model had sharp corners both just behind the nose at the slat and at the main airfoil nose. In the calculations these corners were smoothed out to facilitate the mapping. The two cases had different slat settings as indicated in the figure. Because of the large viscous effects in the test results and uncertainties in the experimental angles of attack the calculations were made for angles of attack which gave a reasonable agreement with the experimental results.

The experiments are seen to indicate substantial separated regions in both cases on the slat lower surface behind the corner close to the nose. The calculated high suction peaks in this region are dashed, because they just reflect the local curvature in the smoothing of the corner. The discrepancy in the shape of the main airfoil upper surface pressure distributions is mainly due to the combined effect of the slat wake and the upper surface boundary layer, which ends in something close to separation at the trailing edge.

In Fig. 7 the calculated supersonic regions are shown for the case in Fig. 6.

The experimental results shown in Fig. 8 are taken from rather old tests with a slatted NACA 64A010[13]. The slat lower surface is seen to be separated behind the nose region as in the previous cases, while the viscous effects on the main airfoil are moderate, partly due to the relatively low Mach number.

To see the effect of a more slender slat the configuration in Fig. 8 was modified, mainly on the slat lower surface, and two cases were run at $M_\infty = 0.5$ and 0.7, Figs. 9 and 10. The pressure distributions obtained for the slat lower surface are seen to be accordingly modified, reducing the risk for boundary layer separation there.

As an example of a trailing edge flap flow Fig. 11 shows the calculation results for a flow with free stream Mach number 0.6 around a NACA 0012 with a flap of the same type and a chord length of 0.25 (main airfoil chord units). The flap angle was 15° and its leading edge was located in $x = 1$, $y = -0.025$.

6. Concluding remarks

The present method has demonstrated its capability of solving the full potential equation with accurate boundary conditions for transonic flowfields around two-element configurations. The solution process will be speeded up by the introduction of mesh refinement capability and, if it proves to work, some acceleration procedure similar to that in Ref. 6.

The viscous effects constitute a greater problem for two-element airfoil systems than in the single airfoil case. Although systems working effectively in transonic flow will not have large separated regions, displacement effects of merged boundary layers on modern supercritical airfoils will be large enough to motivate a further development of the analysis methods. In the present case a suitable approach, which would not involve the mapping procedure, might be to modify the boundary conditions. Instead of zero normal flow a wall outflow is prescribed, proportional to the rate of increase in the displacement thickness, a technique which has been effective for single airfoils.

When viscous corrections are included the potential equation should be solved in fully conservative form. However, in a transonic method giving really good agreement with experiments for a wide class of configurations, an effective shock wave-boundary layer interaction model must be included, which still has to be developed.

References

1. Murman, E.M. and Cole, J.D., "Calculation of plane steady transonic flows", AIAA J., vol. 9, no. 1, Jan. 1971.

2. Jameson, A., "Transonic flow calculations for airfoils and bodies of revolution", Aerodynamics Report 390-71-1, Grumman Aerospace Corp., 1971.

3. Garabedian, P.R. and Korn, D.G., "Analysis of transonic airfoils", Comm. Pure and Appl. Math., vol. 24, pp. 841-851, 1971.

4. Caughey, D.A., "An inviscid analysis of transonic, slatted airfoils", AIAA Paper No. 74-541, 1974.

5. Arlinger, B.G., "Calculation of transonic flow around axisymmetric inlets", AIAA J., vol. 13, no. 12, Dec. 1975.

6. Caughey, D.A. and Jameson, A., "Accelerated iterative calculation of transonic nacelle flowfields", AIAA Paper No. 76-100, 1976.

7. Ives, D.C., "A modern look at conformal mapping, including doubly connected regions", AIAA Paper No. 75-842, 1975.

8. Grossman, B. and Melnik, R.E., "The numerical computation of the transonic flow over two-element airfoil systems", Paper at 5th Int. Conf. on Num. Meth. in Fluid Dynamics, Enschede, The Netherlands, 1976.

9. Murman, E.M., "Analysis of embedded shock waves calculated by relaxation methods", AIAA J., vol. 12, no. 5, 1974.

10. Jameson, A., "Transonic potential flow calculations using conservation form", Proc. AIAA 2nd Comp. Fluid Dynamics Conf., Hartford, Conn., 1975.

11. Ludford, G.S.S., "The behaviour at infinity of the potential function of a two dimensional subsonic compressible flow", J. of Math. Phys., vol. 30, pp. 131-139, 1951.

12. Jameson, A., "Iterative solution of transonic flows over airfoils and wings, including flows at Mach 1", Comm. Pure and Appl. Math., vol. 27, pp. 283-309, 1974.

13. Axelson, J.A. and Stevens, G.L., "Investigation of a slat in several different positions on a NACA 64A010 airfoil for a wide range of subsonic Mach numbers", NACA TN 3129, 1954.

Appendix

Calculation of DF in Eq. (25)

The operator D defined in Eq. (26) may be written

$$D = a^2 D_L + D_q \qquad (A1)$$

where D_L is the Laplace operator

$$D_L = \frac{\partial^2}{\partial r^2} + \frac{1}{r}\frac{\partial}{\partial r} + \frac{1}{r^2}\frac{\partial^2}{\partial \theta^2} \qquad (A2)$$

and

$$D_q = -q_1^2 \frac{\partial^2}{\partial r^2} - \frac{2q_1 q_2}{r}\frac{\partial^2}{\partial r \partial \theta} - \frac{q_2^2}{r^2}\frac{\partial^2}{\partial \theta^2} + \frac{q_2^2}{r}\frac{\partial}{\partial r} \qquad (A3)$$

F consists, according to Eq. (27), of the 4 terms f_1 to f_4 defined in Eqs. (13),(14),(18) and (22), of which f_3 does not contribute to DF. The calculation of Df_4 is straightforward, so only $D(f_1 + f_2)$ is considered here.

Because f_1 is a harmonic function one obtains

$$D(f_1 + f_2) = D_q f_1 + a^2 D_L f_2 + D_q f_2 \qquad (A4)$$

The first and second order derivatives of f_1, needed for the first term in (A4) and for the velocity components, etc., may be written

$$f_{1r} = \frac{a_1}{\sigma^4}(c_1 g_1 + s_1 g_2) \qquad (A5)$$

$$f_{1\theta} = \frac{a_1 r}{\sigma^4}(c_1 g_2 - s_1 g_1) \qquad (A6)$$

$$f_{1rr} = \frac{1}{\sigma^2}\left[-2(r - r_\infty \cos\theta) f_{1r} + 2 r_\infty \sin\theta \frac{1}{r} f_{1\theta}\right] \qquad (A7)$$

$$f_{1r\theta} = \frac{1}{\sigma^2}\left[-2 r r_\infty \sin\theta f_{1r} - (r^2 - r_\infty^2)\frac{1}{r} f_{1\theta}\right] \qquad (A8)$$

$$f_{1\theta\theta} = \frac{r}{\sigma^2}\left[(r^2 - r_\infty^2) f_{1r} - 2 r_\infty \sin\theta f_{1\theta}\right] \qquad (A9)$$

where

$$g_1 = 2 r r_\infty - (r^2 + r_\infty^2)\cos\theta$$

$$g_2 = -(r^2 - r_\infty^2)\sin\theta$$

The constants a_1, c_1 and s_1 are defined in Eqs. (12),(16a) and (16b) and σ, the distance to the infinity point, in Eq. (17).

The corresponding derivatives of f_2 may be written

$$f_{2r} = -h_2 r_\infty \sin\theta \qquad (A10)$$

$$f_{2\theta} = h_2 r (r - r_\infty \cos\theta) \qquad (A11)$$

$$f_{2rr} = 2\frac{h_2}{h_1} r_\infty \sin\theta\left[r - r_\infty \cos\theta - M_\infty^2 \frac{T}{r}(T - r_\infty s_1)\right] \qquad (A12)$$

$$f_{2r\theta} = h_2 r_\infty\left(-\cos\theta + \frac{2\sin\theta}{h_1} h_3\right) \qquad (A13)$$

$$f_{2\theta\theta} = h_2 r\left[r_\infty \sin\theta - \frac{2(r - r_\infty \cos\theta)}{h_1} h_3\right] \qquad (A14)$$

with

$$h_1 = S^2 + \beta^2 T^2$$

$$h_2 = \beta \frac{\Gamma_s + \Gamma_m}{2\pi}\frac{1}{h_1}$$

$$h_3 = r r_\infty \sin\theta - M_\infty^2 T(S + c_1 r_\infty)$$

$$\beta = \sqrt{1 - M_\infty^2}$$

The functions S and T are defined in Eqs. (15a) and (15b).

Finally, for the Laplacian operating on f_2 the expressions above give

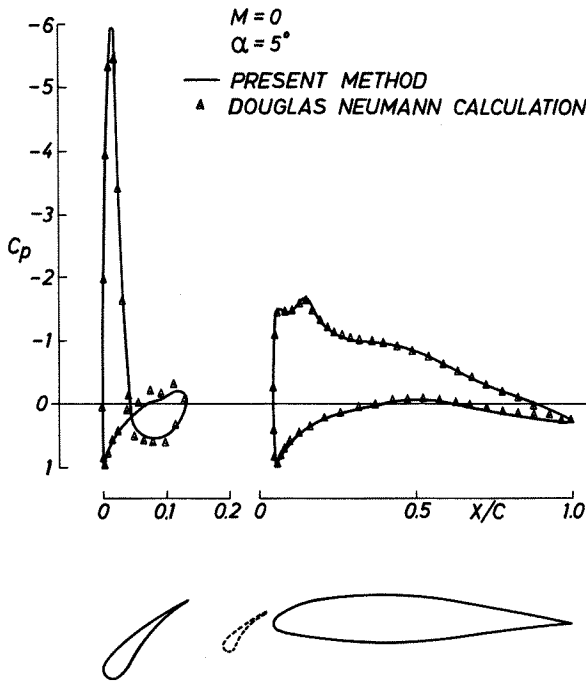$$D_L \, f_2 = 2 \, M_\infty^2 \, ST \, \frac{h_2}{h_1} \qquad \text{(A15)}$$

Fig. 4 Pressure distributions in incompressible flow around NACA 65_2-215 with leading edge slat.
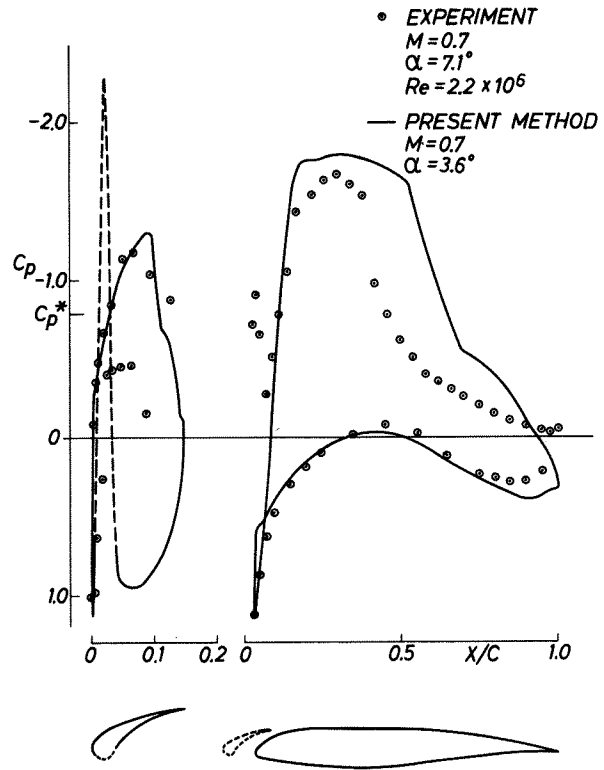

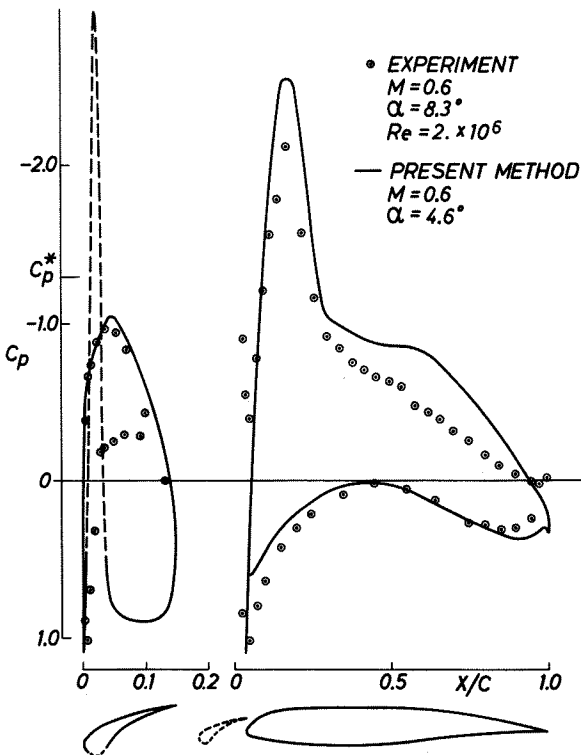Fig. 6 Pressure distributions on airfoil F1.1 with leading edge slat.

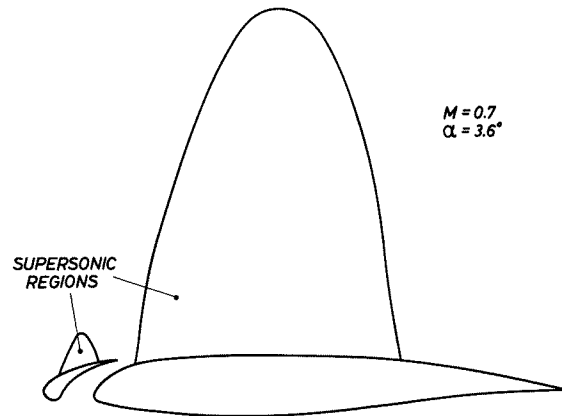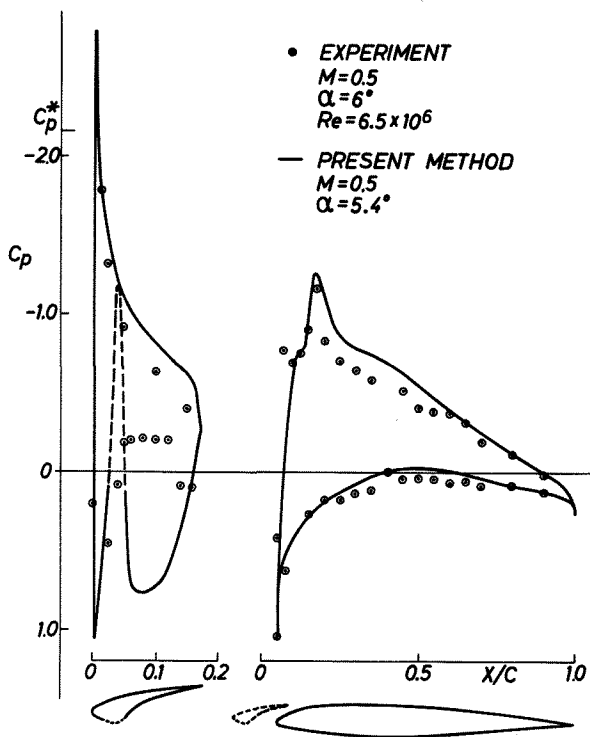Fig. 5 Pressure distributions on airfoil F1.1 with leading edge slat.

Fig. 7 Calculated supersonic regions for airfoil F1.1 with leading edge slat.

Fig. 8   Pressure distributions on NACA 64A010
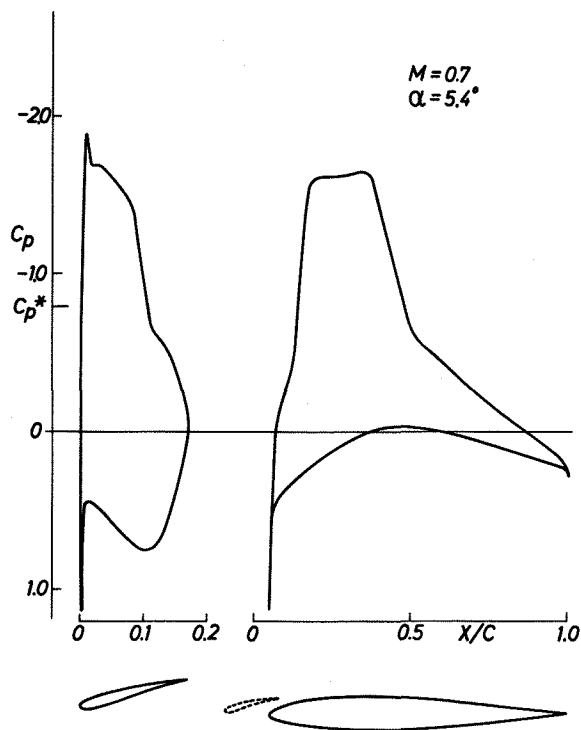with leading edge slat.

Fig. 10   Calculated pressure distribution on
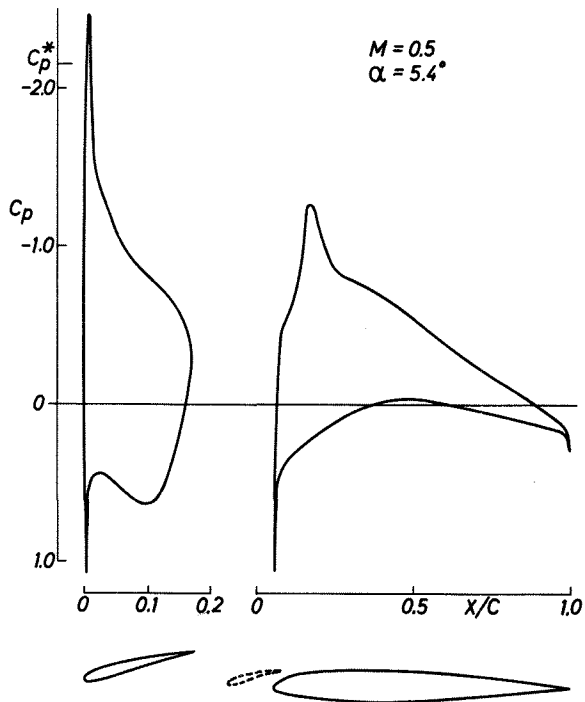NACA 64A010 with modified leading edge
slat.

Fig. 9   Calculated pressure distribution on NACA
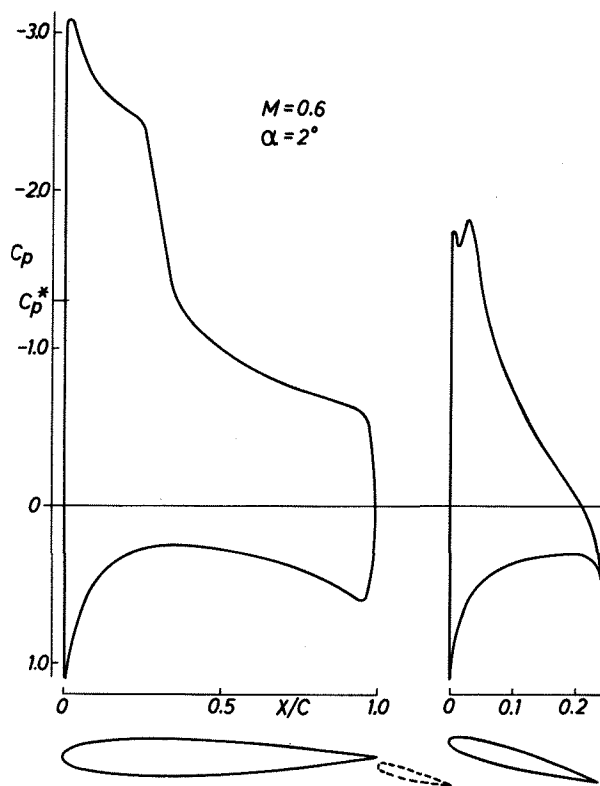64A010 with modified leading edge slat.

Fig. 11   Calculated pressure distribution on
NACA 0012 with NACA 0012 trailing edge
flap.

133